Proceedings World Geothermal Congress 2020+1
Reykjavik, Iceland, April - October 2021

Numerical Modeling of Production Scenarios for Engineered Geothermal System (EGS) in Acoculco, Mexico

Paromita Deb[1], Dominique Knapp[2], Gabriele Marquart[1], Christoph Clauser[1]

[1]Institute for Applied Geophysics and Geothermal Energy, RWTH Aachen University (Germany)

[2]Geophysica Beratungsgesellschaft mbH, Germany

pdeb@eonerc.rwth-aachen.de

Keywords: Acoculco, Enhanced Geothermal Systems, stochastic simulation, production scenario

ABSTRACT

Acoculco has been identified as a potential site for an EGS (Enhanced/Engineered Geothermal System) in Mexico. Within the Horizon 2020 project GEMex, it is investigated as an exploration field. In the present study, we describe the initial steady-state thermal modeling for Acoculco using stochastic forward simulations. We focus on the impact of uncertain input parameters such as thermal conductivity and porosity on the reservoir temperature at different target depths prior to production. Uncertainty is quantified in a Monte Carlo approach, using the algorithm of Sequential Gaussian Simulation (SGS). From the stochastically parametrized model, we extract the mean temperature of our target reservoir rocks from the ensembles of possible realizations. Following this, we analyze the likelihood of success of an EGS in this field by evaluating production scenarios from two different target reservoir rocks, skarn and granite. Simulations are performed using the existing wells as a geothermal doublet. These simulations investigate the impact in the temperature and pressure fields as a result of different injection rates, permeability, and volume of stimulated zone for a production period of 30 years. This study does not attempt to address the technicalities associated with designing a stimulation concept in this field, but rather focuses on the effect of production on the temperature and pressure field considering that a stimulation treatment has successfully resulted in a productive geothermal doublet.

1. INTRODUCTION

Acoculco is one of the exploration geothermal areas in Mexico located in the eastern part of the Trans-Mexican Volcanic Belt. Previous geological studies indicate that this site was subjected to two distinct and major hydrothermal events, which created the Tulancingo – Acoculco caldera complex (Lopez-Hernandez et al., 2009). This geothermally active zone attracted the attention of the Comisión Federal de Electricidad (CFE), the state-owned electric company, due to the extensive surface manifestations observed in the form of acid springs, hydrothermal alteration and gas discharges. CFE drilled two exploration wells in this area, in 1995, EAC-1 and in 2008, EAC-2. Figure 1 shows the location of Aoculco town in a relief map of Mexico (left) and, zoomed-in, the location of the exploration wells, EAC-1 and EAC-2 (right). Both wells are vertical, around 1900 meters deep and have a maximum temperature of around 300 °C at that depth (Pulido, 2010).

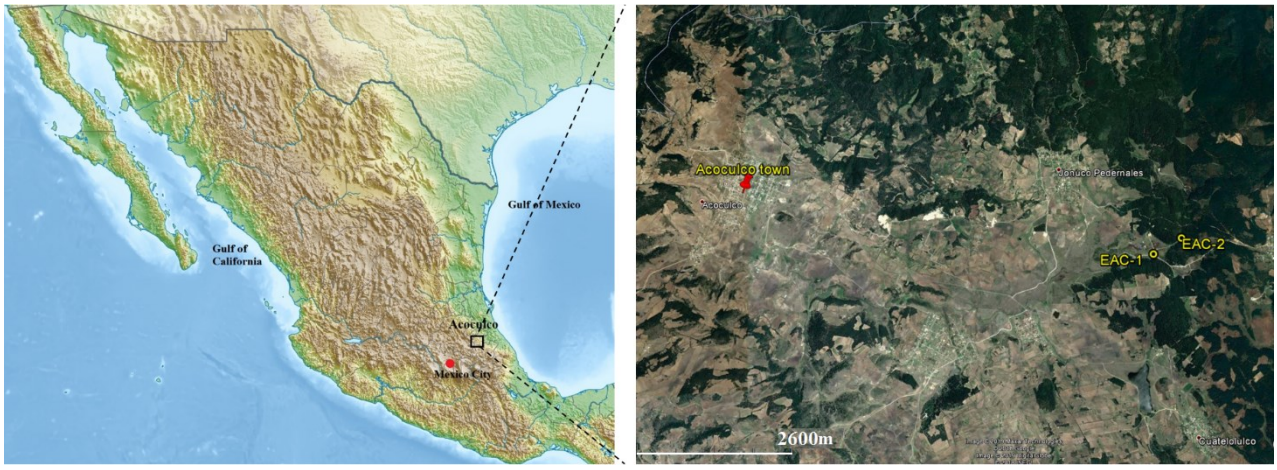

Figure 1: Left: Relief map of Mexico* showing the location of Acoculco field (black square box), Mexico city is shown with a red dot for reference; Right: Google Earth image showing location of Acoculco town and wells EAC-1 and EAC-2

Knowledge of the subsurface lithology in this area is limited to information obtained from these two boreholes. The main lithologic units of well EAC-1 and EAC-2, derived from drill cuttings, consist of volcanic rocks resting on a thick metamorphic sequence. This sequence, made up of skarn and marble is a product of contact metamorphism due to the emplacement of Mid-Tertiary granitic intrusions into the Cretaceous limestone of Sierra Madre Oriental (Lopez-Hernandez et al., 2009, Pulido, 2010). These granitic intrusions are not exposed at the surface, but are intersected by both wells. Well information combined with surface geology and a geological map of Avellán et al. (2018) is used to build a simplified geometrical conceptual model of Acoculco area (Calcagno et al., 2018). Table 1 shows the main lithological units modeled in Acoculco.

**Relief map of Mexico – licensed under https://creativecommons.org/licenses/by/3.0/deed.en*

Table 1: Main lithologic units and rock description

Unit	Rock description	Age (10^6 a)
U1 Volcanites and alluvium	Rhyolitic ignimbrites and lava flows, andesites, basalts (pre-, syn- and post-caldera), alluvial deposits	2.6 to present
U2 Contact aureole	Marble and skarns, aplite dykes	2 – 1
U3 Granite intrusion	Hornblende granite	2 – 1
U4 Sedimentary basement	Jurassic and Cretaceous limestones, argillite limestones, shales	140 – 250

2. TEMPERATURE DATA

Temperature and pressure logging was performed in both EAC-1 and EAC-2 wells. The available data for EAC-1 and EAC-2 comprises of temperature logs at regular intervals of 6, 12, 18 and 24 hours of drilling and pressure logs after 6 and 24 hours of drilling for EAC-1 and after 18 and 24 hours of drilling for EAC-2. Additionally, heating up surveys performed after 12 and 13 days of heating for both temperature and pressure for EAC-1, indicate that the borehole temperature reached a stable condition (Figure 2, left). According to CFE drilling reports, EAC-1 suffered no significant circulation losses during drilling. Interestingly, well EAC-2, located less than 500 meters east of EAC-1, encountered circulation losses of around 20 m^3/h – 30 m^3/h at a depth 1840 m. Temperature data points measured at this depth immediately after drilling show a slope change indicating a possible feed zone. However, this observation is based on only two temperature data points from data logged immediately after drilling and hence not conclusive (Figure 2, right). Based on these observations, CFE classified Acoculco geothermal field as a Hot Dry Rock system characterized by high temperature and low permeability.

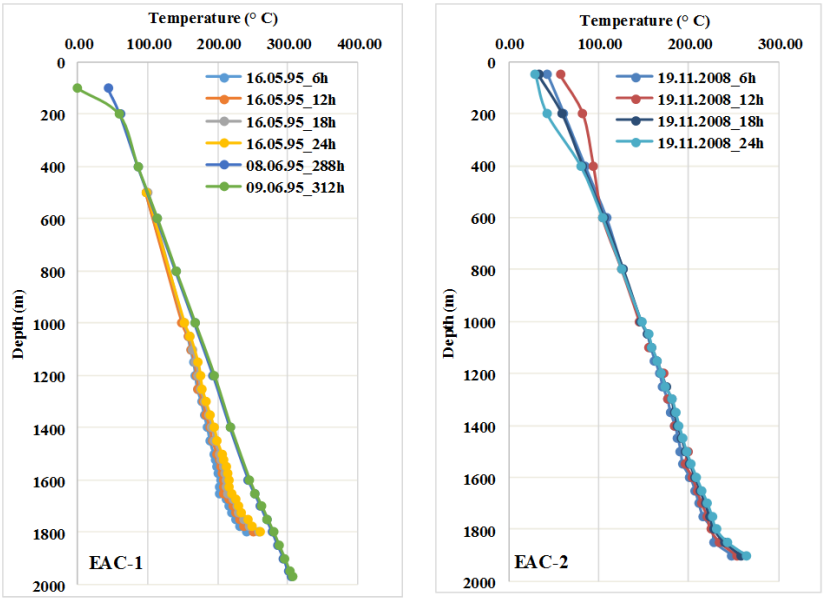

Figure 2: Temperature logs of EAC-1 (left) and EAC-2 (right), different colors indicate different times of measurement

3. NUMERICAL MODEL

3.1 Model approach

With anomalous high temperatures observed in two exploratory wells, Acoculco is expected to have great potential of geothermal energy production. However, the field is currently in exploration stage and requires better subsurface understanding to quantify its potential

We focus on two aspects in this paper. Firstly, we study the initial steady-state temperature of the field. We develop petrophysical and thermal models of Acoculco to obtain an initial estimate of the potential resource within the caldera complex. The preliminary structural model with major lithological units is parameterized with representative rock properties. These are based on laboratory measurements performed on outcrop analogues (Table 2). As a consequence, there is great uncertainty regarding the rock properties. This has several reasons, namely the lack of a calibration based on core measurements, the fact that measurements are performed on altered and weathered samples, possible sampling errors, etc. Considering these basic problems associated with outcrop measurements, we focus on the effect of uncertain rock properties (thermal conductivity and porosity) on the modeled formation temperature using a stochastic approach.

Secondly, we make a preliminary evaluation of Acoculco as a potential EGS site by simulating production scenarios from potential reservoir rocks in the existing doublet.

3.2 Governing equations

For numerical simulation the finite differences code SHEMAT-Suite is used (Rath et al., 2006, Clauser, 2003).

The steady-state mass conservation of water in a porous medium is expressed by the continuity equation, where h represents the hydraulic head, Q the source and sink term, **k** the permeability tensor, ρ_f and μ_f density and dynamic viscosity of the pore fluid, respectively, and g gravity:

$$\nabla \cdot \left(\frac{\rho_f g}{\mu_f} \boldsymbol{k} \nabla h \right) + Q = 0 \tag{1}$$

The physical properties of water in sub-critical and super-critical conditions are calculated using the correlations provided by the International Association for the Properties of Water and Steam (Wagner et al., 2000). The pore water pressure (P) is calculated according to the vertical head distribution and the depth z where P_0 represents the pressure at the surface for z=0:

$$P(z,h) = P_0 + \int_0^z \rho_f(\tilde{z}) g (h - \tilde{z}) d\tilde{z}. \tag{2}$$

Heat transport due to conduction, advection and radiogenic heat production is expressed by the steady-state conservation equation:

$$(\rho c)_f \mathbf{v} \nabla \mathrm{T} - \nabla \cdot (\lambda_e \nabla T) = A. \tag{3}$$

The equation consists of an advective term, with specific discharge **v**, fluid density ρ_f and fluid specific heat capacity c_f, a diffusive term, with the effective thermal conductivity of the rock-fluid mixture λ_e, assumed to be isotropic, and a heat generation term A.

Groundwater flow and specific discharge **v** are described by Darcy's Law:

$$\mathbf{v} = \frac{k}{\mu_f} (\nabla p - \rho_f g \nabla z). \tag{4}$$

Rock thermal conductivity depends on the rock type but generally decreases with temperature (Zoth and Hänel, 1988). To account for the dominant igneous and magmatic rock components within the model domain, we implemented the correction proposed Sekiguchi (1984). The formula implements the temperature correction for matrix thermal conductivity λ_m based on a given matrix conductivity at room temperature $\lambda_{m,0}$ and the temperature T in Pasquale's et al. (2017) notation:

$$\lambda_m = 1.8418 + (\lambda_{m,0} - 1.8418) \left(\frac{1}{0.002732\, T + 0.7463} - 0.2485 \right). \tag{5}$$

Effective thermal conductivity of the fluid filled porous rock λ_e depends on porosity, fluid thermal conductivity λ_f and rock matrix thermal conductivity λ_m. It is calculated according to the geometric mean (i.e., Clauser, 2003):

$$\lambda_e = \lambda_f^{\phi}\, \lambda_m^{(1-\phi)}. \tag{6}$$

For transient simulations in the stimulated reservoir volume, the following formulations are implemented in the code SHEMAT-Suite.

To calculate the pressure within the wells $P_{w,}$ we use the semi-analytical approach by Peaceman (1983) to convert the corresponding numerical grid block pressures P_b to well pressures:

$$P_w = P_b - \frac{q_w \mu_f}{2\pi k \Delta z} ln \left(\frac{r}{r_w} \right). \tag{7}$$

With volume flow rate, q_w [$m^3\ s^{-1}$], fluid dynamic viscosity, μ_f [Pa s], magnitude of permeability, k [m^2], vertical discretization of the corresponding grid cell in z-direction, Δz [m], and well radius r_w [m]. The parameter r is the equivalent cell radius. For a cubic cell with isotropic permeability and equal grid size in x and y direction, the original formulation by Peaceman (1983) can be simplified to

$$r = 0.14\sqrt{2}\Delta x. \tag{8}$$

From the mean pressures at the injector and the producer, reservoir impedance, *i* can be calculated using the average pressures at the producer and injector and the production flow rate q_w

$$i = \frac{P_{injector} - P_{producer}}{q_w}. \tag{9}$$

Reservoir impedance reflects the pressure difference needed to circulate a fluid volume through the stimulated permeable zone (e.g., Kolditz and Clauser, 1998). The reservoir impedance should not exceed 100 kPa s L^{-1} to ensure economic feasibility of the project (Clauser, 2006).

3.3 Thermal model

In the Acoculco caldera complex, the major regional fault systems are identified based on alignment of surficial structures like volcanic cones. The two dominant fault patterns recognized in this area are the NW-SE trending damaged zones and the NE-SW oriented normal fault system. Minor E-W trending faults associated with the Acolculco caldera evolution are also reported (Lopez-Hernandez et al., 2009). The fault structures, associated with regional stress patterns are modelled in one of GEMex work packages (WP 3) and are shown in Figure 3 (left). The extent of the reservoir model of Acoculco used for performing stochastic simulations is outlined with the blue boundary in Figure 3. The model has a dimension of 16 km × 17 km × 3.5 km and the deepest vertical limit coincides with mean sea level referenced as zero km in the model domain. Figure 3b shows the numerical grid from SHEMAT-Suite with the main structural units and the granitic intrusion at the center (in red). The grid cells are equal-sized with a dimension of 150 m × 150 m × 50 m, yielding a total of 846 370 cells. All simulations assume that heat conduction is the primary heat transfer process as the geothermal field is characterized by low permeability.

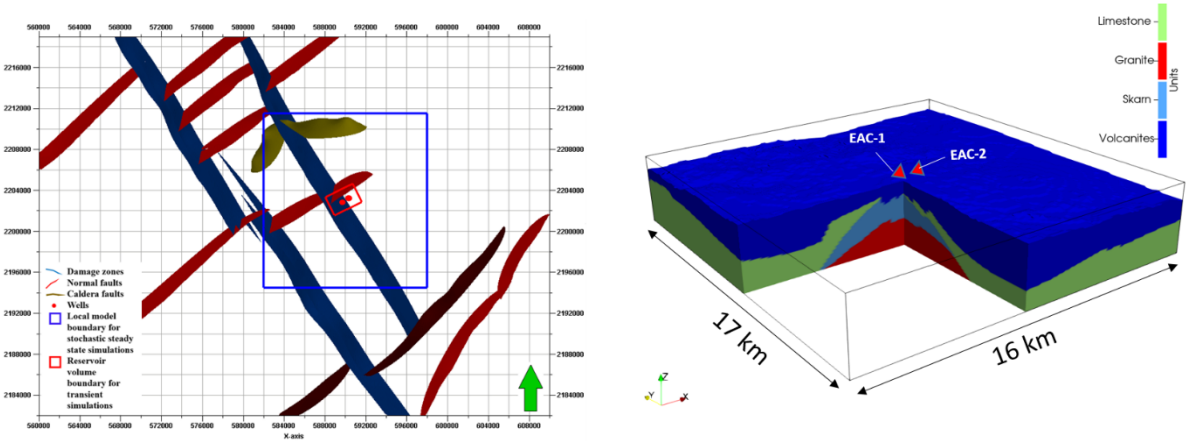

Figure 3: Left: Modelled faults in the Acoculco area, NE-SW trending normal faults (red), NW-SE trending damaged zones (blue) and almost E-W trending caldera faults (green), EAC-1 and EAC-2 wells are indicated by the red dots, the blue square outlines the reservoir model used for stochastic simulation while the red rectangle indicates the extent of the reservoir volume used for evaluating production scenarios (Section 4); Right: reservoir model showing different structural units (colors are indexed in the right corner)

3.3.1 Stochastic parameters

To evaluate the impact of uncertainties of thermal conductivity and porosity on the formation temperature we perform steady-state numerical Monte Carlo simulations in the reservoir model (Figure 3). To this end, the physical properties such as thermal conductivity and porosity are treated as randomly distributed. Laboratory measurements yield mean and standard deviations of matrix thermal conductivity and porosity for the main rock units. We assumed normal distribution of the parameters within the rock types and synthetically sampled 1000 values per parameter as input for the Sequential Gaussian Simulation. Table 2 provides the rock property values used as input for the different rock types.

Table 2: Petrophysical properties of rock units obtained from laboratory measurements on outcrop samples

Units	Rock type	Porosity [%]		Thermal Conductivity (matrix) $\left[\frac{W}{m\,K}\right]$		Permeability (matrix) [m²]		Heat generation rate $\left[\frac{\mu W}{m^3}\right]$	Volumetric Heat Capacity $\left[\frac{W}{m^3\,K}\right]$	
		Mean	Std.Dev.	Mean	Std.Dev	Mean	Std.Dev	Mean	Mean	Std.Dev
1	Volcanites	11.20	2.02	2.50	0.19	3.03×10^{-16}	6.93×10^{-16}	1.13	2104819	134023
2	Limestones	1.17	1.40	2.90	0.26	2.02×10^{-18}	2.30×10^{-18}	0.62	2080855	16538
3	Marble and Skarn	1.22	0.60	3.89	0.60	2.15×10^{-18}	2.04×10^{-18}	0.62	2625176	52138
4	Granite	2.00	-	3.20	-	3.00×10^{-18}	-	2.45	2730075	534374

In addition to rock property histograms, spatial correlation lengths are essential parameters for stochastic simulation. The lack of petrophysical well-log data or any other kind of geophysical data (e.g., seismic) limits reliable estimation of vertical and horizontal correlation lengths. In absence of spatial geological correlation lengths, we investigated different scenarios to understand the impact of different correlation lengths on the temperature field. For each scenario, an ensemble of 500 realizations is generated by performing steady-state stochastic forward simulations assuming reasonable correlation lengths in vertical and horizontal directions. We extracted the mean ensemble temperatures at the top and bottom of each geological unit for wells EAC-1 and EAC-2 for different scenarios and compared them. The effect of correlation length on the mean ensemble temperature turns out to be negligible. Detailed discussions

on stochastic simulation parameters and results are not a part of this study and hence we limit ourselves to using the results of the stochastic simulations.

For numerical modeling, the heat boundary condition is kept identical under both the wells. We assigned a constant specific heat flow of 360 mW m^{-2} under the granite intrusion outline and 91 mW m^{-2} under the adjacent area as boundary conditions at the bottom of our domain. The top is fixed at a constant temperature of 12 °C implemented as boundary condition for the stochastic simulations.

3.3.2 Uncertainties in temperature

The Monte Carlo approach enables generating an ensemble of realizations of the subsurface model. Each realization is equally likely and respects the input data and a-priori geological knowledge. In the Acoculco geothermal field, where hard data for a calibration of models is limited to the temperature profiles from two wells, a deterministic approach towards thermal modeling is quite uncertain. Using the 500 realizations of the subsurface model and comparing the spread in the simulated temperature helps to understand the impact of variation in each parameter. In this discussion, we present the results of the stochastic simulations where we simultaneously varied both thermal conductivity and porosity based on the rock property histograms generated from measured data.

Figure 4 shows the profiles of the simulated temperatures for wells EAC-1 (left) and EAC-2 (right). The colored lines are the profiles extracted from 500 different realizations performed by varying both thermal conductivity and porosity stochastically. The realizations are compared to the measured stabilized bottom hole temperature (indicated by black triangles) of wells EAC-1 and EAC-2.

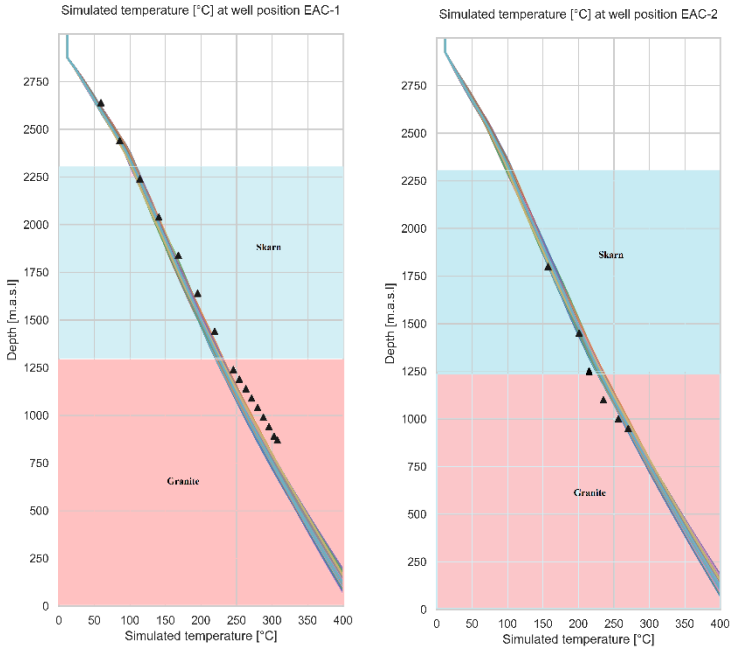

Figure 4: Temperature profiles for EAC-1 (left) and EAC-2 (right) obtained from 500 stochastic realizations, the black triangles are the measured stabilized borehole temperatures at corresponding depths, skarn and granite sections are highlighted.

For ease of discussion, the skarn and granite units are highlighted in Figure 4. The temperature gradient in the skarn section based on measurements is 132 mK m^{-1} in EAC-1 and around 110 mK m^{-1} for EAC-2. The difference in thermal gradient between these two wells becomes more pronounced when we compare the gradients in granite. The gradient calculated from the measured stabilized temperature data within the highlighted granite section is around 164 mK m^{-1} for well EAC-1 but increases to around 230 mK m^{-1} for EAC-2. Table 3 highlights the results of the stochastic simulation, indicating the mean ensemble temperature and corresponding standard deviation obtained from 500 realizations for the top and bottom temperature of the skarn reservoir and the granite reservoir. The average temperature gradient within the skarn unit computed from the mean ensemble temperature of the two wells is 116 mK m^{-1} while that computed for the granite unit increases to 145 mK m^{-1}. This significant change in temperature gradient within the granite section between wells, which are, only few hundred meters apart can only be explained either by a possible local heat anomaly close to well EAC-2.

We use the stochastically derived mean temperature values presented in Table 3 for simulating production scenarios within the skarn and the granite sections of EAC-1 and EAC-2, presented in the next section.

Table 3: Mean ensemble temperatures at assumed stimulation depths obtained from stochastic simulation, the temperatures for specific depths are mean values of temperatures extracted at well positions EAC-1 and EAC-2

Position of evaluation	Mean ensemble temperature [°C] (std. dev. [K]) (calculated from 500 realizations)
Skarn reservoir top [2400 m.a.s.l.]	91.25 (1.26)
Skarn reservoir bottom [1650 m.a.s.l.]	179.62 (1.56)
Granite reservoir top [1300 m.a.s.l.]	222.83 (1.70)
Granite reservoir bottom [550 m.a.s.l.]	332.10 (2.17)

4. EGS POTENTIAL IN ACOCULCO

Enhanced or engineered geothermal system implies creating a stimulated/fractured zone as a result of reactivation and connection of existing fractures and faults thereby establishing flow between a borehole doublet. The technicalities of engineering permeability in a geothermal reservoir at depth is not within the scope of this study. Here, we simulate production scenarios assuming that stimulation in the pre-existing wells, EAC-1 and EAC-2 is successful. Considering the very high temperature gradient observed in the skarns as well as the granites, both of these units are potential targets for stimulation. Therefore, we simulate the effect of production on the thermal field for two production scenarios defined by two target reservoir rocks, skarn and granite. Well EAC-1 serves as an injector and EAC-2 as a producer. For this purpose, we extract reservoir volumes of dimension 3 km × 2 km ×1 km from the stochastically parameterized local model at two different target locations. One volume targets the skarn reservoir from a depth of 2400 m.a.s.l. (450 m from surface) to 1650 m.a.s.l. (1200 m from surface) The other one targets the granite from a depth of 1300 m.a.s.l. (1550 m from surface) to 550 m.a.s.l., (2350 m from surface) respectively. We refine the grid size of the extracted reservoir volume towards the well positions to account for the higher fluid velocities near the producer and injector. Grid dimensions in x- and y-directions are varying between 10 m and 142 m, respectively, while the discretization in z-direction is held constant at 20 m. We present results only from the simulations performed using the Skarn reservoir volume. A schematic example for the skarn reservoir is shown in Figure 5.

In the following sections, we define the geometry and the hydraulic properties of the stimulated zone within the two reservoir volumes and use those parameters to perform transient simulation for a production period of 30 years

4.1 Geometry of the stimulated zone

The geometry and extent of the stimulation zones depend strongly on the regional and local stress patterns, pre-existing weakness in the rock and the stimulation techniques. In this study, we consider hydraulically created stimulated zones of a maximum horizontal extent of 1200 m for each well. This horizontal extent ensures connectivity between the two wells, which are 550 m apart from each other to form an effective geothermal doublet. This stimulated zone is represented as a three-dimensional rectangular volume with a width of 100 m in the numerical model. We scale the associated permeability accordingly so that the resulting volumetric flow rate is the same as a single planar fracture and its associated damage zones.

The vertical extent of the stimulated volume is varied to investigate the impact of different volumes of the stimulation zone. Two different scenarios with a vertical extent of 100 m and 300 m are used for this study, however it should be noted that these values might still correspond to very conservative assumptions of fracture length or fracture networks.

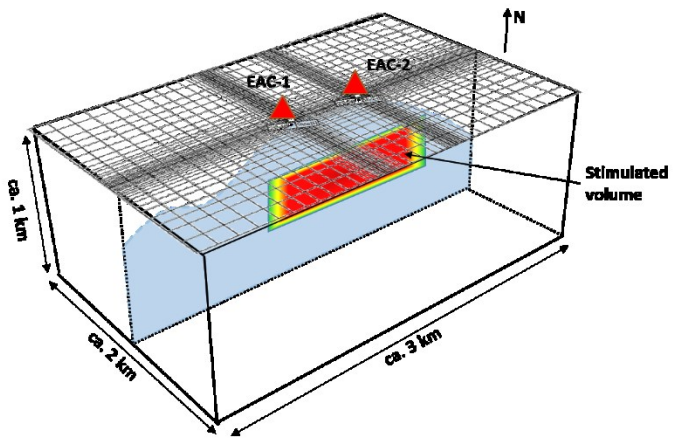

Figure 5: Schematic figure showing example of variable gridding in reservoir volumes: fine gridding approaching the well location and coarser gridding away from the well, well locations at the surface are shown using the red triangles, a cross section showing the central stimulated area as a rectangular shaped zone (in red) within a skarn reservoir volume (in blue)

4.2. Hydraulic properties

Results from the stochastic simulation in the larger model are used to define the temperature boundary conditions for the stimulated volumes. The top and bottom of the two reservoir volumes are assigned a Dirichlet temperature boundary condition with the mean temperature obtained from the stochastic realizations (Table 3): for the skarn reservoir, temperatures of 91.25 °C at the top and 179.62 °C at the bottom of the domain. Prior to the production scenarios, an undisturbed temperature field for the reservoir models is obtained by running a steady-state simulation.

To compare the effect of permeability, we evaluate scenarios with two different permeability values applied to the central stimulated zone, 10^{-12} m² and 10^{-13} m². Permeability of less than 10^{-13} m² for the stimulation zone results in numerical instability due to the pressure drop between producer and injector. As we move away from the central stimulation zone, we decrease permeability by one order of magnitude for the first 40 m, followed by a decrease of two orders of magnitude in the next 20 m and, finally, reduce to 10^{-15} m² at the zone borders. Similar permeability values have been evaluated in other EGS systems. For example, in Soultz-Sous-Forêts, the permeability range estimated is in the order of 10^{-12} m² to 10^{-14} m² (corresponding approximately to 1 Darcy – 10 Millidarcy) decreasing from the stimulation centre to the edges (Vogt et al., 2012).

Table 4: Model properties for transient simulations on skarn reservoir volumes

Model size	3000 × 2000 × 1100 m^3
Mesh size	61 × 40 × 55 m^3
Resolution	x: 10 m – 142 m y: 10 m – 135 m z: 20 m
Stimulated volumes	1150 × 100 × 100 m^3 1150 × 100 × 300 m^3
Temperature at reservoir top	91.25 °C
Temperature at reservoir bottom	179.62 °C
Simulation time	30 Years
Permeability	10^{-12} m^2, 10^{-13} m^2
Circulation rate	10 L s^{-1}, 30 L s^{-1}, 50 L s^{-1}
Temperature of injected water	70 °C (EAC-1)
Constant fluid dynamic viscosity*	2.06×10^{-4} Pa s (@ 135 °C)
Constant fluid density*	935.59 kg m^{-3} (@ 135 °C)
Constant fluid specific heat capacity*	4248 J kg^{-1} K^{-1} (@ 135 °C)
Constant fluid thermal conductivity*	0.69 W m^{-1} K^{-1} (@ 135 °C)

All simulations are tested for three circulation rates, 10 L s^{-1}, 30 L s^{-1} and 50 L s^{-1} (constant over time) to understand the impact of injection rates on the temperature distribution with time. This range covers the lower end of flow rates established in operating EGS reservoirs (e. g. Vogt et al., 2012) as well as an economically acceptable flow rate (50 L s^{-1}). The injection temperature is set to 70 °C to inhibit mineral precipitation and clogging of the injection wells (Li and Lior, 2014). For all simulations, we assume 100 % water recovery and no loss to the formation. As SHEMAT-Suite allows only a volume input and volume extraction of water at the injector and the producer cells, the fluid properties of the extracted and injected water (density, specific heat capacity and fluid dynamic viscosity) are set constant, adjusted to the mean reservoir temperature at stimulation depth. The model properties are listed in Table 4.

4.3. Results and discussion on the production scenarios

The following section presents the simulated thermal and hydraulic behavior for different production scenarios of for the fractured reservoir within skarn considering two vertical extents of the fractured zone, 100 m and 300 m, representing two different fracture volumes. In addition, we test the response in temperature and pressure on two different permeability values of the central simulated zone, 10^{-12} m^2 and 10^{-13} m^2.

4.3.1. Stimulation in skarn

Figure 6 shows exemplarily the variation of reservoir temperature with time for production from a stimulated zone in Skarn over a period of 30 years using different flow rates and permeability for vertical extents of the fracture zone of 100 m (left) and 300 m (right). For 100 m, i.e. a central stimulated volume of 0.012 km^3 (= 100 m × 100 m × 1200 m), a very early thermal breakthrough is observed after almost 1 year of operation for higher production rates of 30 L s^{-1} and 50 L s^{-1} (Figure 6, left). The temperature falls below 80 °C within 10 years of production. For a production rate of 10 L s^{-1}, the temperature decline begins after 2 years of production and stabilizes at around 95 °C after 20 years.

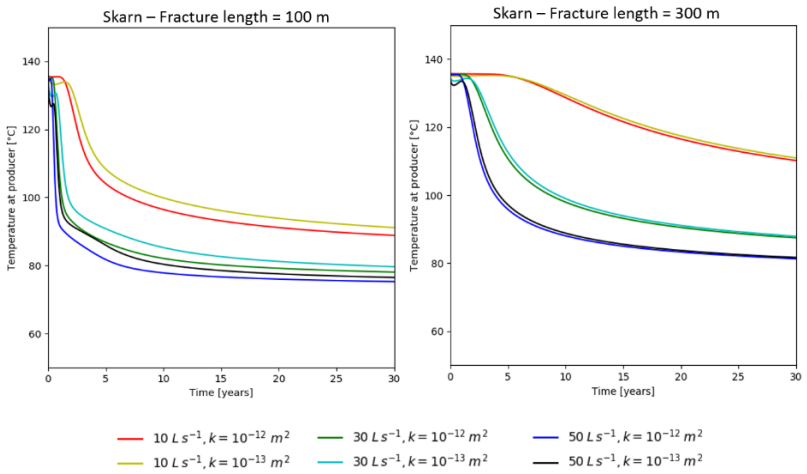

Figure 6: Temperature vs. time for production from Skarn for different flow rates, permeability and fracture lengths

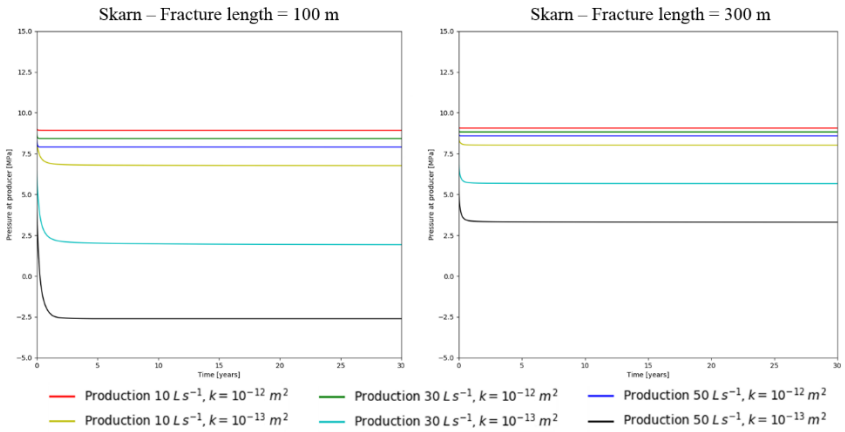

Figure 7: Pressure vs. time for producer at different flow rates and permeability values for the Skarn reservoir

However, in case of the larger stimulated volume of 0.036 km^3 (= 100 m × 300 m × 1200 m), with an production rate of 10 L s^{-1}, the thermal breakthrough occurs much later, starting only after 7-8 years of production (Figure 6, right). Temperature does not decrease below 110 °C after 30 years of production. As expected, a faster temperature decline takes place with increasing production rate. For an economically acceptable production with an injection and production rate of 50 L s^{-1}, temperature stabilizes at around 85 °C after 30 years of production. It is to be noted that for the larger stimulated zone, the effect of permeability is not as strong as in the case of the smaller stimulated volume.

Figure 7 illustrates the variation of well pressure with time in response to the production. For scenarios with lower permeability (10^{-13} m²), we observe a sharper decline in pressure with increasing flow rate as compared to scenarios with higher permeability (10^{-12} m²). This trend is common for both small and large stimulated volumes. However, the overall pressure decay in case of the smaller fractured volume is stronger than in the scenario with the larger fractured volume. This pressure response strongly reflects the impact of the stimulated volume.

Another important parameter deciding the commercial feasibility of a reservoir is the reservoir impedance (Eq. 9). Its value should not exceed 100 kPa s L^{-1} (e.g., Clauser, 2006) for an economic case. In Table 5, we present the reservoir impedance values calculated for different production scenarios for the skarn reservoir. For the two scenarios with a permeability of 10^{-12} m², the reservoir impedance lies within a feasible range for both small and big reservoir volumes. However, for the low permeability scenario with 10^{-13} m², it exceeds the threshold value of 100 kPa s L^{-1}, indicating less feasible scenarios for an economic production.

Table 5: Reservoir Impedance for different simulated volumes and permeability in Skarn

Reservoir scenario	Permeability [m²]	Circulation rate [L s^{-1}]	Reservoir Impedance [kPa s L^{-1}]
Skarn small reservoir	10^{-12}	10/ 30/ 50	57.71/ 57.90/ 58.19
Skarn small reservoir	10^{-13}	10/ 30/ 50	532.67/ 535.91/ 533.33
Skarn large reservoir	10^{-12}	10/ 30/ 50	25.38/ 25.42/ 25.50
Skarn large reservoir	10^{-13}	10/ 30/ 50	248.33/ 249.10/ 249.95

CONCLUSION:

Valuation of asset and decision making in a geothermal exploration field requires quantification of uncertainty of critical parameters such as temperature and pressure. This work demonstrates a workflow, which can be applicable to other exploration fields with little and highly uncertain input data. In this work, we provide an initial estimate of the temperature distribution and its uncertainty (in terms of ensemble standard deviation) associated with underdetermined properties of the Acoculco geothermal reservoir. Additionally, we investigate the efficiency of skarn reservoir rock as an EGS stimulation target and provided exemplary temperature and pressure responses for different hydraulic parameters for a production period of 30 years. The scenarios are based on assumptions of realizable reservoir permeability in the order of 10^{-12} m^2 to 10^{-13} m^2.

We assumed ad-hoc synthetic stimulation volumes of 0.012 km^3 and 0.036 km^3. It is, however, uncertain to what extent a possible pre-existing fracture network can be reactivated by a hydraulic stimulation at Acoculco to form an efficient high permeability zone for a geothermal doublet. Stimulation tests such as mini-fracking in existing wells may provide reliable estimates of stress direction and magnitude. These are essential before any stimulation program can be designed for the wells.

The current preliminary investigations, however, suggest that the assumed stimulated volumes within Skarn may not be sufficient for commercial purposes. Larger fracture volumes need to be achieved so that the injected water has sufficient time to become hot. A connection to high-permeability fault features might optimize the pressure built-up and drop between the wells and allow for an efficient mixture and heating-up of the injected fluids.

ACKNOWLEDGEMENT:

We thank the Comision Federal di Electricidad (CFE) for providing data and information regarding their geothermal wells and the entire GEMex consortium comprising of Mexican and European partners for the cooperation and unpublished inputs on conceptual ideas, which are used for this study.

REFERENCES

Avellán, D.R., Macías, J.L., Layer, P. W., Cisneros, G., Sánchez - Núñez, J.M., Gómez-Vasconcelos, Pola, A., Sosa-Ceballos, G., García-Tenorio, F., Reyes-Agustín, G., Osorio-Ocampo, S., García-Sánchez, L., Mendiola, F., Marti, J., López-Loera, H., and Benowitz, J, 2018, Geology of the Late Pliocene – Pleistocene Acoculco caldera complex, eastern Trans-Mexican Volcanic Belt (México), *Journal of Maps*, https://doi.org/10.1080/17445647.2018.1531075.

Calcagno, P., Evanno, g., Trumpy, E., Gutiérrez-Negrín, L. C., Macías, J. L., Carrasco-Núñez, G., Liotta, D., 2018. Preliminary 3-D geological models of Los Humeros and Acoculco geothermal fields (Mexico) – H2020 GEMex Project., *Advances in Geosciences, 45,* 321 – 333.

Clauser, C., ed., 2003. *Numerical Simulation of Reactive Flow in Hot Aquifers. SHEMAT and PROCESSING SHEMAT,* Springer, New York.

Clauser, C., 2006. Geothermal energy. In: Heinloth, K., (ed.). Landolt-Börnstein, Group VIII: Advanced Material and Technologies, Vol. 3: Energy Technologies, Subvol. C: Renewable Energies. Springer Verlag, Heidelberg-Berlin.

Kolditz, O., Clauser, C., 1998. Numerical simulation of flow and heat transfer in fractured crystalline rocks: application to the hot dry rock site in Rosemanowes (U.K.), *Geothermics, 27(1),* 1-23.

Li, Mengying., Lior, Noam., 2014. Comparative analysis of powerplant options for Enhanced geothermal Systems (EGS). *Energies*, 7, 8427 – 8445, doi: 10.3390/en7128427

López-Hernándes, A., García-Estrada, G., Aguirre-Díaz, G., González-Partida, E., Palma-Guzmán, H., Quijano-Léon, J. L., 2009. Hydrothermal activity in the Tulancingo-Acoculco Caldera Complex, central Mexico: Exploratory studies. *Geothermics, 38,* 279 – 293.

Peaceman, D.W., 1983. Interpretation of well-block pressure in numerical reservoir simulation with non-square grid blocks and anisotropic permeability, *Society of Petroleum Engineers Journal, 23(3)*, 531-543.

Pulido, C. L., Flores Armenta, M., Ramírez Silva, G., 2010. Characterization of the Acoculco Geothermal Zone as HDR System. *GRC Transactions, 34 (2010).*

Rath, V., Wolf, A., Bücker, M., 2006. Joint three-dimensional inversion of coupled groundwater flow and heat transfer based on automatic differentiation: sensitivity, calculation, verification, and synthetic examples, *Geophys. J. Int., 167,* 453 – 466.

Sekiguchi, K., 1984. A method for determining terrestrial heat flow in oil basin areas. *Tectonophysics, 103,* 67 – 79, Elsevier Science Publishers B. V. Amsterdam – Netherlands.

Vogt C., Marquart, G., Kosack, C., Wolf, A., Clauser, C., 2012. Estimating the permeability distribution and its uncertainty at the EGS demonstration reservoir Soultz-sous-Forêts using the ensemble Kalman filter, *Water Resources Research, 48,* W08517, doi: 10.1029/2011WR011673.

Wagner, W., Cooper, J., Dittmann, A., Kijima, J., Kretzschmar, H., Kruse, A., Mares, R., Oguchi, K., Sato, H., Stocker, I., Sifner, O., Takaishi, Y., Tanishita, I., Trubenbach, J., Willkommen, T., 2000. The IAPWS industrial formulation 1997 for the thermodynamic properties of water and steam. *J Eng Gas Turbines Power Trans ASME. 2000, 122(1),* 150–82. doi:10.1115/1.483186.

Zoth, G., Hänel, R., 1988. Appendix: 10.1. Thermal Conductivity. In: Hänel, R., Rybach, L., Stegna, L., (eds.), Handbook of terrestrial heat flow density determination, Kluwer Academic Publishers, Dordrecht, pp 447 – 468.